Insight into the antiferromagnetic structure manipulated by electronic reconstruction

B. Cui,[1] F. Li,[1] C. Song,[1,*] J. J. Peng,[1] M. S. Saleem,[1] Y. D. Gu,[1] S. N. Li,[1] K. L. Wang,[2] and F. Pan[1,†]

[1]*Key Laboratory of Advanced Materials (MOE), School of Materials Science and Engineering, Tsinghua University, Beijing 100084, China*

[2]*Department of Electrical Engineering, University of California, Los Angeles, California 90095, USA*

(Received 8 June 2016; revised manuscript received 28 July 2016; published 3 October 2016)

Antiferromagnetic (AFM) materials, with robust rigidity to magnetic field perturbations and ultrafast spin dynamics, show great advantages in information storage and have developed into a fast-emerging field of AFM spintronics. However, a direct characterization of spin alignments in AFM films has been challenging, and their manipulation by lattice distortion and magnetic proximity is inevitably accompanied by "ferromagnetic" features within the AFM matrix. Here we resolve the *G*-type AFM structure of $SrCoO_{2.5}$ and find that the interfacial AFM structure could be modulated intrinsically from in plane to out of plane with a canted angle of 60° by the charge transfer and orbital reconstruction in $SrCoO_{2.5}/La_{2/3}Sr_{1/3}MnO_3$ heterostructures both experimentally and theoretically. Such an interfacial AFM reconfiguration caused by electronic reconstruction does not cause the ferromagnetic feature and changes the magnetization switching process of $La_{2/3}Sr_{1/3}MnO_3$ from in plane to perpendicular to the plane, in turn. Our study not only reveals the coupling between charge, orbital, and AFM structure, but also provides a unique approach to manipulating AFM structure.

DOI: 10.1103/PhysRevB.94.134403

I. INTRODUCTION

Giant (tunneling) magnetoresistance stands out as a seminal phenomenon in the emerging field of spintronics [1]. In the spin valve or magnetic tunnel junction, the antiferromagnetic (AFM) layer is used as a fundamental static supporting material to establish a reference magnetization direction [2]. Recently, beyond the passive role of AFM materials as a pinning layer, great efforts are made to control the antiferromagnet in the emerging field of AFM spintronics due to its negligible ferromagnetic (FM) stray field and rigidity to magnetic field perturbations [3–6]. Compared with FM and AFM metals, correlated oxides with strong interaction between lattice, charge, spin, and orbital degrees of freedom provide a wonderful arena for the manipulation of spin structure of magnetic oxides [7].

In correlated oxides, the FM spins have been successfully tuned by the four degrees of freedom: epitaxial strain and corresponding lattice variation modulate magnetic phase transition [8], charge transfer results in interfacial magnetism [9,10], spin realignments induce exchange bias [11], and orbital reconstruction causes magnetic anisotropy [12]. The situation turns out to be different in the world of AFM materials. Although the AFM spins have been shown to be affected by the lattice-distortion-induced FM-AFM phase transition [8] and FM proximity-induced interfacial spin canting [13], these two elements (e.g., lattice and spin) inevitably break the pristine spin state of AFM, accompanied by the emergent FM feature in the AFM matrix, rather than an intrinsic modulation of AFM structure. Based on the symmetry, now the research interest is whether the other two elements, charge and orbital, could manipulate AFM structure intrinsically, providing a unique opportunity to encode a rich spectrum of exotic states in oxide heterostructures [7].

Among various AFM systems, *G*-type AFM (*G*-AFM) materials with a distinctive compensated configuration exhibit delicate physics such as multiferroics, but make the source of exchange coupling at the FM/*G*-AFM interface confusing because the canted angle of interfacial AFM structure in Dzyaloshinskii-Moriya (DM) interaction lacks directly experimental characterization [11,14,15]. Here we use x-ray absorption spectroscopy (XAS), x-ray magnetic linear dichroism (XMLD), and x-ray linear dichroism (XLD) combined with first-principles calculations to resolve the AFM structure manipulated by charge transfer and orbital reconstruction in the heterostructure of FM $La_{2/3}Sr_{1/3}MnO_3$ (LSMO) and *G*-AFM $SrCoO_{2.5}$ (SCO). Such an electronic reconstruction causes an interfacial out-of-plane AFM structure with a canted angle of 60° and does not introduce the FM feature. The AFM reconfiguration also changes the magnetization switching process of $La_{2/3}Sr_{1/3}MnO_3$ from in plane to perpendicular to the plane in turn. Our results not only build a physical image for *G*-AFM structure, but also offer a broad opportunity to tailor the AFM materials.

II. METHODS

The SCO (*t*)/LSMO (6 nm) heterostructures were grown epitaxially on (001) $SrTiO_3$ (STO) substrates using pulsed laser deposition (PLD), where the thicknesses of SCO vary from 0 to 80 nm. The LSMO was grown at 750 °C with an oxygen pressure of 200 mTorr while SCO was grown at 870 °C with an oxygen pressure of 10 mTorr, and the heterostructures were cooled to room temperature in 2 Torr to stabilize the stoichiometry of $SrCoO_{2.5}$. The films were patterned into an orthogonal Hall-bar device with an effective length of 400 μm and a width of 100 μm to measure the magnetoresistance in the channel perpendicular and parallel to the magnetic field.

A Quantum Design superconducting quantum interference device (SQUID) measurement system (QD MPMS-7) was used to measure the magnetic properties. The transport properties were carried out in a physical property measurement system (PPMS). The dependence of resistance on the magnetic

*songcheng@mail.tsinghua.edu.cn

†panf@mail.tsinghua.edu.cn

field (H) was measured by sweeping H in plane, while the angle dependence of resistance was measured by rotating the device out of plane with a fixed magnetic field of 2.5 kOe. The exchange bias in the magnetization and transport measurements was introduced by cooling the samples down to 10 K with a magnetic field of 2 kOe.

The XAS, XMLD, and XLD measurements were performed in total electron yield (TEY) mode at the Beamline BL08U1A in Shanghai Synchrotron Radiation Facility (SSRF) at 300 K. For the measurements of AFM structure in SCO, the XMLD is the difference of two XAS curves with horizontal and vertical polarizations. In all the XAS measurements, a constant background was fitted to the pre-edge region of the L_3 edge and subtracted from the spectra, which were then normalized to the edge jump to unity above the L_2 edge. The sample could be rotated in plane and out of plane to detect the AFM structure. Differently, in the measurements of orbital occupancy in LSMO (XLD), the polarization directions of the linearly polarized x rays are tuned by rotating the x-ray incident angle (the angle between the x ray and the surface of the film plane), with 90° and 30° corresponding to in plane ($E \parallel a$) and majority of out of plane ($E \parallel c$), respectively. The spectra normalization was made by dividing the spectra by a factor so that the L_3 pre-edge and L_2 post-edge have identical intensities for the two polarizations. After that, the pre-edge spectral region was set to 0, while the peak at the L_3 edge was set to 1 [12].

First-principles calculations were carried out with the projector augmented wave implementation of the Vienna *ab initio* simulation package (VASP). Generalized gradient approximation plus U (GGA + U) was used as the energy function, with a setting of the Coulomb repulsion (U) and the exchange interaction (J) for d electrons; that is, $U = 3$ eV and $J = 0.98$ eV for Mn and $U = 4.5$ eV and $J = 1.0$ eV for Co [16,17]. In the calculation, a $\sqrt{2} \times \sqrt{2} \times 6$ lattice was used for $La_{2/3}Sr_{1/3}MnO_3$, and a $\sqrt{2} \times \sqrt{2} \times 4$ lattice was used for $Sr_2Co_2O_5$, while similarly a sequence of $(CoO/SrO/CoO_2/SrO)_2/MnO_2/LaO/MnO_2/SrO/MnO_2/LaO$ with a vacuum layer of 20 Å was used for LSMO/SCO. An initial magnetic moment along [100] crystal direction with a small out-of-plane component is set on the Mn in SCO/LSMO due to the enhanced out-of-plane orbital occupancy of LSMO at the interface. All the structures are optimized with a cutoff energy of 600 eV and appropriate k-point meshes which were both increased until convergence.

The micromagnetic simulation is carried out in a LSMO sample using three-dimensional (3D) object-oriented micromagnetic framework (OOMMF). The simulation is carried out in a LSMO sample size of $20 \times 80 \times 2\,nm^3$ with a cubic cell of $2 \times 2 \times 2\,nm^3$ and the magnetic field is applied in the in-plane x axis. Input parameters for LSMO include saturation magnetization $M_S = 270 \times 10^3$ A/m, exchange stiffness A=1.94 $\times 10^{-12}$ J/m, and biaxial anisotropy constant $K = -1.5 \times 10^4$ J/m^3 [18,19]. According to the resolved AFM structure in XMLD, the interfacial G-type AFM structure of the SCO layer is introduced by adding a FM materials layer of $20 \times 80 \times 2\,nm^3$ on the top of LSMO with a very large perpendicular magnetic anisotropy and magnetic field in the z axis and the magnetization directions of adjacent cells are opposite.

III. RESULTS AND DISCUSSIONS

A. Evolution of AFM structure in SCO/LSMO

Magnetization curves along the [100] direction at 10 K for SCO (t = 0, 2, 4, 8, 10, 20, 30, 40, 60, and 80 nm)/LSMO (6 nm) heterostructures with a cooling field of 2 kOe [inset of Fig. 1(a)] are measured and the thickness dependences of the coercivity (H_C) and exchange bias field (H_{EB}) are summarized in Fig. 1. Remarkably, the growth of AFM SCO brings about a shift of the loop along the magnetic field axis towards negative fields followed by a simultaneous enhancement of H_C and H_{EB} due to the formation of AFM domain structure [20]. The values of H_C and H_{EB} increase abruptly from 30 to 789 Oe and 0 to 133 Oe, respectively, as t increases from 0 to 40 nm. Then the further increase of t to 80 nm does not alter the magnetic properties significantly, suggesting that the AFM structure of SCO is stable when $t > 40$ nm.

Using these samples with different SCO thicknesses, we could resolve the G-type AFM structure in the whole bulk of the SCO layer by XMLD (the difference between horizontally and vertically polarized XAS) as shown in Fig. 2(a). The XMLD is measured by rotating the sample in plane (solid curves) and out of plane (dot curves). The in-plane angle ω is the angle between the [100] crystalline axis of the substrate and the horizontal polarization direction, while the out-of-plane angle φ is the angle between the surface of the film and the incident x-ray. The intensity of XMLD is determined by the difference between angles of AFM spin/horizontal polarization and AFM spin/vertical polarization: The larger the angle difference is, the stronger the XMLD signal is [21,22]. It is noteworthy that the possible influence of orbital ordering on the XMLD signal in the unstrained $SrCoO_{2.5}$ ($a_{SCO} = a_{STO} = 3.905$ Å) could be excluded due to its fully occupied t_{2g} and empty e_g orbitals as shown in Fig. S1 of the Supplemental Material [23].

In the case of $t = 40$ nm [Fig. 2(b)], the XMLD signal decreases gradually as the in-plane angle ω changes from −45° to 0° and then increases with an opposite sign by rotating ω from 0° to 45°, where the out-of-plane angle φ is fixed at 90°. The sketch for the geometrical relationship among

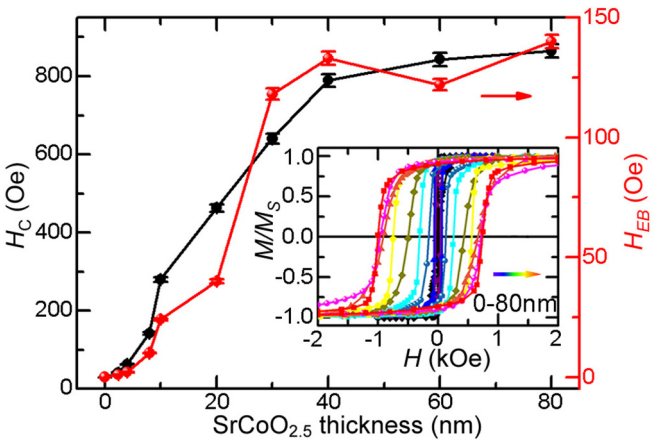

FIG. 1. The dependence of coercivity (H_C, left axis) and exchange bias field (H_{EB}, right axis) on $SrCoO_{2.5}$ thicknesses at 10 K. Inset is corresponding normalized magnetization curves.

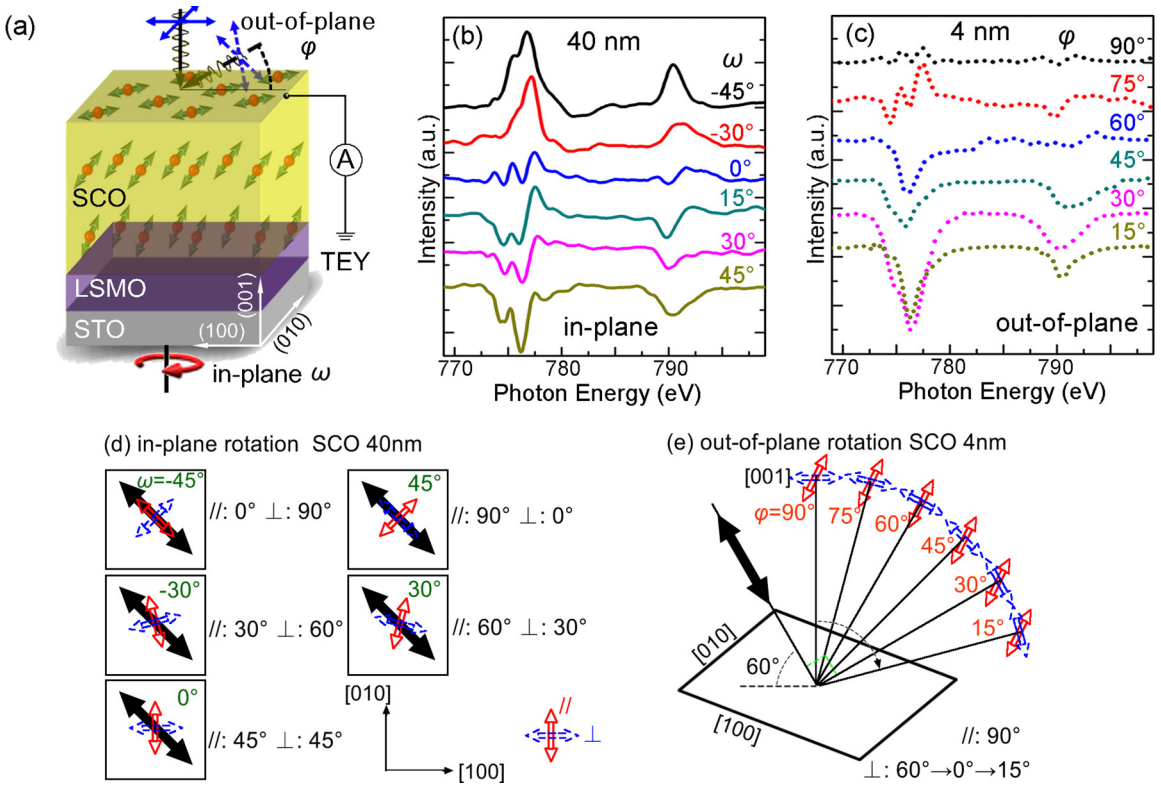

FIG. 2. (a) Schematic of XMLD measurement and AFM structure in SCO with different distances from the interface. Co-XMLD signals for SCO of (b) 40 nm and (c) 4 nm. The solid and dot curves are XMLD signals under different in-plane (ω) and out-of-plane (φ) rotation angles, respectively. The sketch for the geometrical relationship among antiferromagnetic spin (black solid arrows), horizontal ($\parallel$, red hollow arrows with solid frames), and vertical ($\perp$, blue hollow arrows with dashed frames) polarization: (d) in-plane rotation for 40 nm SCO and (e) out-of-plane rotation for 4 nm SCO. The angles' values of ω, φ, AFM spin/horizontal polarization ($\parallel$), and AFM spin/vertical polarization ($\perp$) are marked.

AFM spin (black solid arrows), horizontal (hollow arrows with solid frames), and vertical (hollow arrows with dashed frames) polarization is shown in Fig. 2(d), where the angles of AFM spin/horizontal polarization ($\parallel$) and AFM spin/vertical polarization ($\perp$) are marked. The enhancement of XMLD signal with the absolute value of ω increases from 0° to 45° demonstrates that the AFM spins are arranged along the [110] crystal direction, because the angle differences gradually change from 90° to −90° as ω changes from −45° to 45°. Such an AFM structure does show an obvious out-of-plane component (Fig. S2(a) in [23]), which is in consistent with the previous theoretical work [16]. Note that the AFM structure given by XMLD is mainly for the area near the surface, taking the attenuation depth of total electron yield (TEY) mode (∼6 nm) into consideration [12].

The situation changes dramatically for the interfacial AFM structure in the heterostructures by reducing the thickness of SCO to 4 nm. Different from the similar signal intensity for $\omega = 0°$ to 45°(Fig. S2(b) in [23]), with the out-of-plane rotation from $\varphi = 90°$ to 30° (ω is fixed at 45°), the XMLD signals of this sample are monotonously increased in Fig. 2(c). However, a further decrease of φ to 15° reduces the intensity of XMLD, indicating that the AFM spin has a ∼60° canted moment. According to the geometry of polarizations, AFM spin of SCO (4 nm)/LSMO is shown in Fig. 2(e). When the AFM spin is arranged out of plane with a canted angle of 60° and incident x ray is rotated out of plane from 90° to 15° [Fig. S1(b)], the angle between AFM spin and horizontal polarization maintains 90°, while the angle between AFM spin and vertical polarization changes from 60° ($\varphi = 90°$) to 0° ($\varphi = 30°$) and then 15° ($\varphi = 15°$). Thus the angle difference increases from 30° to 90° and then back to 75°, resulting in the enhanced XMLD intensity from $\varphi = 90°$ to 30° and reduced XMLD intensity from $\varphi = 30°$ to 15°. The out-of-plane AFM spin has a ∼60° canted moment to guarantee nonlinear interfacial AFM/FM moments for the realization of exchange coupling based on DM interaction [24,25]. Note that the AFM structure in ultrathin SCO is similar to the interface area of thick SCO (Fig. S3 in [23]).

We then turn to investigate the dependence of AFM spin on the thickness of the SCO layer. The situation for $t = 20$ nm is similar to that of the case of $t = 40$ nm as shown in Fig. 3(a) and in Fig. S2(c) in the Supplemental Material [23], suggesting that the preferred AFM structure in the bulk area of SCO is along [110]. The enhancement of XMLD with the increase of out-of-plane rotation angle is observed when the thickness of SCO increases to 8 nm in Fig. 3(b). Nevertheless the in-plane rotation from 45° to 0° would reduce the signal intensity (Fig. S2(d) in [23]), which illustrates that the AFM structure in the case of 8 nm also exhibits a strong in-plane component and the critical thickness for the canted out-of-plane AFM structure should be less than 8 nm. The dependences of

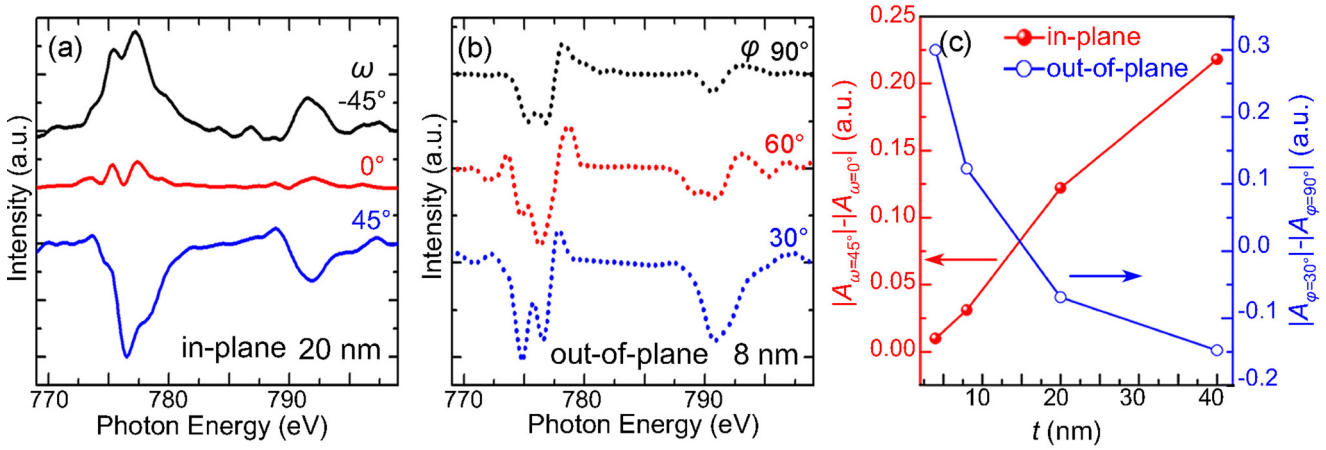

FIG. 3. Co-XMLD signals for SCO of (a) 20 nm and (b) 8 nm. The solid and dot curves are XMLD signals under different in-plane (ω) and out-of-plane (φ) rotation angles. (c) The dependences of $|A_{\omega=45^\circ}|-|A_{\omega=0^\circ}|$ (left axis) and $|A_{\varphi=30^\circ}|-|A_{\varphi=90^\circ}|$ (right axis) on SCO thickness. A is the integral area of XMLD.

$|A_{\omega=45^\circ}|-|A_{\omega=0^\circ}|$ (left axis, $\varphi = 90^\circ$) and $|A_{\varphi=30^\circ}|-|A_{\varphi=90^\circ}|$ (right axis, $\omega = 45^\circ$) on SCO thickness (t) shown in Fig. 3(c) could be used to estimate the AFM structure, where A is the integral area of XMLD. A higher $|A_{\omega=45^\circ}|-|A_{\omega=0^\circ}|$ value and positive $|A_{\varphi=30^\circ}|-|A_{\varphi=90^\circ}|$ present the in-plane and out-of-plane AFM structures, respectively. When t increases from 4 to 40 nm, the value of $|A_{\omega=45^\circ}|-|A_{\omega=0^\circ}|$ increases and $|A_{\varphi=30^\circ}|-|A_{\varphi=90^\circ}|$ changes from positive to negative. Thus the evolution of the G-AFM structure of SCO in SCO/LSMO with the depth is directly imaged: The AFM spin firstly behaves as a canted out-of-plane moment at the interface area (~4 nm), then turns to be in-plane aligned gradually with the distance departing from the interface (~8 nm), and finally returns to the in-plane [110] crystal axis in the bulk of the film. However, an in-plane AFM structure is demonstrated in a single SCO layer of 4 nm on the STO substrate (Fig. S4), which indicates that the insertion of LSMO plays an important role in determining the interfacial out-of-plane AFM structure.

B. Interfacial electronic reconstruction

We turn to find the origin of interfacial out-of-plane AFM structure in SCO/LSMO by investigating the interfacial electronic reconstruction, as displayed in Fig. 4. Compared with the single layer of SCO, the Co-XAS of SCO (4 nm)/LSMO shifts to a lower-energy direction as marked by the arrow in Fig. 4(a), suggesting that the valence of Co is reduced at the interface between LSMO and SCO [26]. Correspondingly, the valence of Mn at the interface is higher than that of the single LSMO layer, reflected by the shift of Mn-XAS of SCO/LSMO to the high-energy direction in Fig. 4(b) [27]. The variations in the valence of Mn and Co at the interface demonstrate the charge transfer from Mn to Co via the out-of-plane Co-O-Mn covalent bond [27]. Here the possible diffusion between La and Sr might reduce and increase the valences of Co and Mn at interface, respectively, but indeed is not favored by the strain. Compared with LSMO ($a = 3.870$ Å), $SrMnO_3$ ($a = 3.806$ Å)—which is introduced by the diffusion of Sr into LSMO—shows a higher tensile strain on the STO substrate ($a = 3.905$ Å). Meanwhile, the diffusion of La into SCO drives its lattice parameter ($a = 3.905$ Å) away from the unstrained state.

The formation of an interfacial covalent bond is accompanied by the orbital reconstruction as seen in the Mn-XLD curves shown in Figs. 4(c) and 4(d). Different from XMLD, XLD is the difference between XAS with the incident angles of 90° ($E \parallel a$) and 30° ($E \parallel c$) [inset of Fig. 4(c)] [12]. As LSMO grown on a STO substrate is under tensile strain, the preferred orbital is in plane, $d_{x^2-y^2}$, demonstrated by the negative XLD signal around the L_2 peak in the case of single LSMO. Conversely, the positive XLD signal in SCO/LSMO indicates that the electrons prefer to locate at

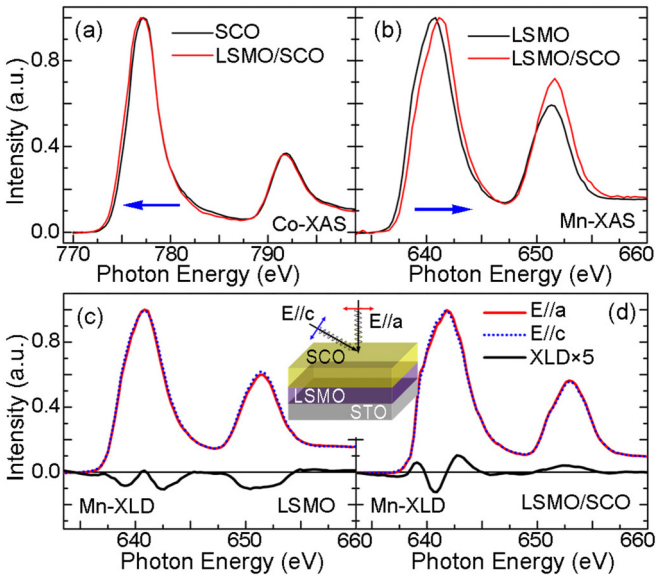

FIG. 4. Normalized (a) Co-XAS for single SCO and SCO (4 nm)/LSMO and (b) Mn-XAS for single LSMO and SCO (4 nm)/LSMO. The arrows mark the shift of SCO (4 nm)/LSMO XAS compared with single-layer samples. Normalized Mn-XAS [photon polarization parallel ($E \parallel a$) and almost perpendicular ($E \parallel c$) to the sample plane] and Mn-XLD signals of (c) single LSMO and (d) SCO (4 nm)/LSMO. The inset of (c) is the sketch of Mn-XLD measurement.

the out-of-plane $d_{3z^2-r^2}$ orbitals with low energy level due to the orbital hybridization across the interface [9,27]. Although the surface symmetry breaking in single LSMO also induces a preferred $d_{3z^2-r^2}$ occupancy, it should not contribute to the orbital reconstruction in SCO/LSMO without the absence of apical oxygen. It is noteworthy that the electron extraction in Mn caused by charge transfer from Mn to Co would weaken the orbital ordering in Mn according to our previous study [12], but it would not change the sign of orbital ordering. Thus the orbital reconstruction from in-plane to out-of-plane orbital ordering in Figs. 4(c) and 4(d) is caused by the formation of the Co-O-Mn covalent bond perpendicular to the interface. Such an out-of-plane orbital reconstruction in LSMO, rather than the proximity effect from the bottom FM layer (Fig. S5 in [23]), should account for the interfacial out-of-plane AFM structure in SCO, similar to the dependence of FM structure on the orbital occupancy [12].

C. First-principles calculations

The modulation of AFM structure caused by electronic reconstruction is also supported by the first-principles calculations in Fig. 5. The dependences of magnetic anisotropic energy (MAE) for SCO on in-plane angle ω' (the angle between AFM spin and [100] crystal direction) and out-of-plane angle φ' (the angle between AFM spin and the surface of sample) are presented in Figs. 5(a) and 5(b), respectively. The MAE of a single SCO layer shows a sinusoidal-like dependence on ω' (φ' is fixed at 90°) with the minimum at 45° and 225°, suggesting that the easy axis for AFM spin in SCO bulk is [110] ([$\bar{1}$10]). Subsequently, the gradual enhancement of MAE with the increase of φ' confirms that the arrangement of AFM spin out of plane is not energetically stable for SCO bulk. The scenario differs dramatically with the introduction of FM LSMO; the amplitude of MAE variation by rotating AFM spins in plane is reduced in the SCO/LSMO heterostructure with a single period from 0° to 360° related to the interfacial DM interaction (Fig. S6 in [23]). The corresponding out-of-plane rotation towards the [001] axis would reduce the MAE of SCO/LSMO in Fig. 5(b) with a minimum energy at $\varphi' = 90°$, in agreement with the canted out-of-plane AFM spin at 60°. These theoretical results are highly in line with the XMLD results for the SCO/LSMO samples with different SCO film thicknesses.

The partial density of states (PDOS) of Co and Mn in SCO, LSMO, and SCO/LSMO is shown in Figs. 5(c) and 5(d), respectively. Compared with the single SCO and LSMO layer, the PDOS of Co and Mn in SCO/LSMO shifts to the negative and positive direction, respectively, suggesting the charge transfer from Mn to Co [Fig. 5(e)] [28], corroborated by the experimental XAS results. The occupancy of each 3d orbital obtained from PDOS demonstrates that such a charge transfer is accompanied by the preferential out-of-plane orbital occupancy (Fig. 6). Figure 6(a) presents the partial density of state for each 3d orbital of the Co atom in the CoO_6 octahedron, for bulk SCO and at the interface of LSMO/SCO, while those of Mn in LSMO and LSMO/SCO are displayed in Fig. 6(b). All the PDOS curves of different 3d orbitals for interfacial Co (Co in LSMO/SCO) shift to a lower-energy direction [Fig. 6(a)], while those for interfacial Mn (Mn in LSMO/SCO)

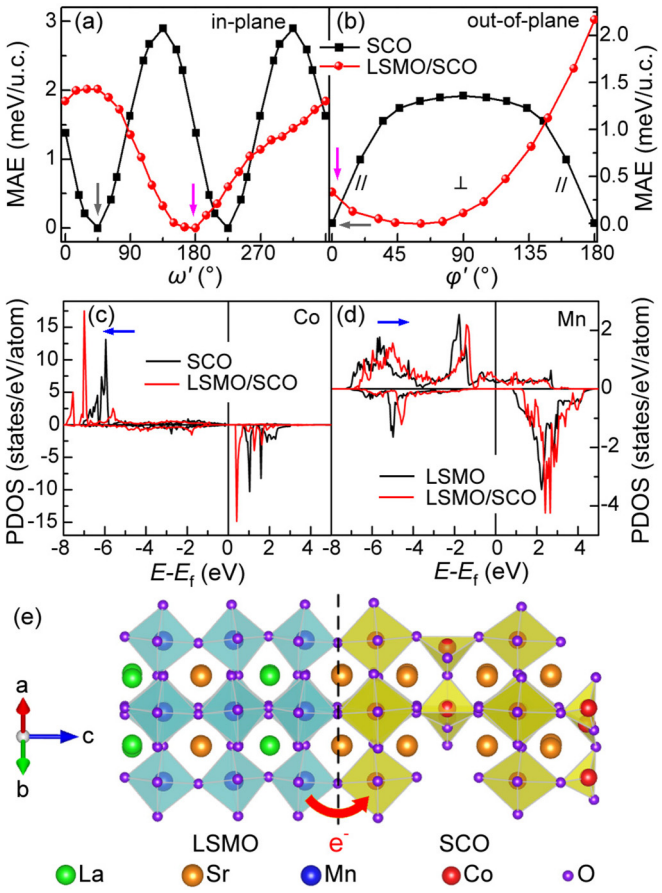

FIG. 5. MAE for AFM spin in SCO and SCO/LSMO with (a) in-plane and (b) out-of-plane rotation. The initial in-plane angle for (b) is the angle with lowest MAE in (a) as marked by the arrows. The PDOS of (c) Co for SCO and SCO/LSMO and (d) Mn for LSMO and SCO/LSMO. The blue arrows indicate the shift direction of PDOS for SCO/LSMO heterostructure compared with the case of single layer. (e) Schematic for the charge transfer at the SCO/LSMO interface.

shift to a higher-energy direction [Fig. 6(b)], compared with corresponding bulk counterparts. These results are in line with the sum of all the orbitals as displayed in Figs. 5(c) and 5(d). We then integrate the PDOS curves below the Fermi level (E_f) to give the evidence for the orbital occupancy modulation at the interface. The integrated areas for all the orbitals with an out-of-plane component of interfacial Co (xz, yz, and $3z^2$–r^2) increase as summarized in Table I, suggesting the formation of an out-of-plane Co-O-Mn bond based on the charge transfer from Mn to Co. The Co-O-Mn bond and corresponding charge transfer also reduce occupancies of all the 3d orbitals of Mn at the interface except for that of the $3z^2$–r^2, corroborated by the experimental XLD results in Figs. 4(c) and 4(d). This is also the reason why we set an out-of-plane FM moment component in LSMO in the calculation of AFM structure energy.

D. Various FM switching driven by different AFM structure

The magnetization switching of the FM layer should be sensitive to the AFM structure [29]. We then address the question whether the interfacial out-of-plane AFM structure would affect the magnetic switching process of SCO/LSMO

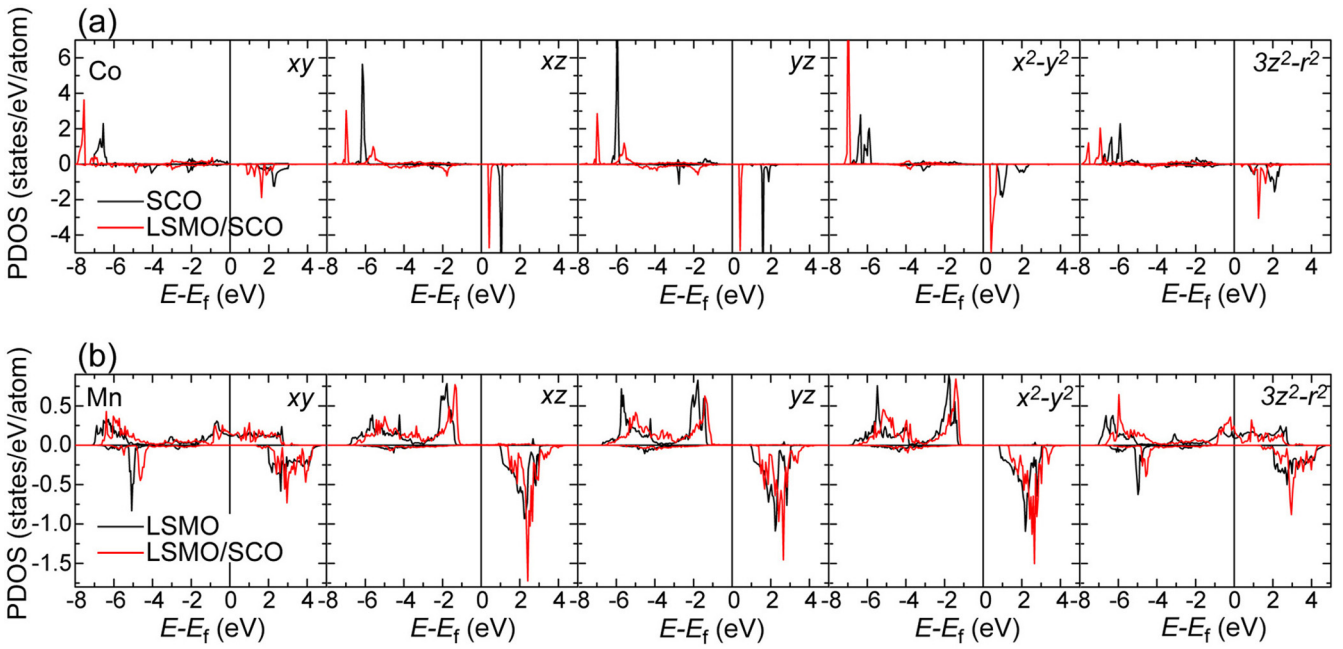

FIG. 6. The PDOS of different 3*d* orbitals for (a) Co in SCO and LSMO/SCO and (b) Mn in LSMO and LSMO/SCO.

in an orthogonal Hall bar, as presented in the inset of Fig. 7(a). The dependence of $R/R_{\min}$ on magnetic field (H) ($R/R_{\min}$-H, left column) was measured with H applied in the plane of devices ($R_{\min}$ is the minimum value of each curve), and the dependence of $R/R_{\min}$ on the out-of-plane rotation angle ($R/R_{\min}$-θ, right column; θ is the angle between H and device plane) was measured under $H = 2.5$ kOe. The resistance of the channel parallel to the magnetic field is defined as R_1 (black), while the perpendicular one is defined as R_2 (red). The most eminent feature observed here is the distinct profile of $R_2/R_{\min}$-H with different SCO thickness. When $t = 40$ nm, $R_2/R_{\min}$-H behaves as dual peaks near the H_C in the left column of Fig. 7(a), which is similar to that of the parallel one ($R_1/R_{\min}$-H). However, as t decreases to 20 nm [the left column of Fig. 7(b)], dual valleys emerge at H_C in $R_2/R_{\min}$-H and become more and more obvious as t further drops to 4 nm, and even 0 nm [the left column of Figs. 7(c) and 7(d)].

Before explaining the changes in magnetoresistance (MR), we need to emphasize that the MR near H_C is closely related to the domain wall scattering and the anisotropic magnetoresistance (AMR) in LSMO films [30,31]. The former one only increases the channel resistance with a peak near the H_C [30], while the relationship of $R_1(\theta = 0°) < R_2(\theta = 0°) < R_1(\theta = 90°) = R_2(\theta = 90°)$ in $R/R_{\min}$-θ [the right column of Figs. 7(a)–7(d)] suggests that the AMR follows the sequence of $R_{\parallel} < R_{\perp-\text{in}} < R_{\perp-\text{out}}$ due to the enhanced in-plane conductivity in tensile strained LSMO [32,33]. $R_{\parallel}$, $R_{\perp-\text{in}}$, and $R_{\perp-\text{out}}$ are the resistances when the current is parallel, in-plane perpendicular, and out-of-plane perpendicular to the magnetization, respectively [30,32]. For $t = 40$ nm, the peak values in $R/R_{\min}$-H are close to the maxima in $R/R_{\min}$-θ ($R_{\perp-\text{out}}$), suggesting that the magnetization switching is realized in an out-of-plane route due to the perpendicular AFM/FM coupling at the interface. With decreasing SCO thickness, although the interfacial out-of-plane AFM structure still exists, the FM/AFM out-of-plane coupling is not robust enough due to the absence of stable AFM bulk structure, consistent with the suppression of H_{EB} in samples with $t < 40$ nm. Thus the magnetization of SCO (4 and 0 nm)/LSMO tends to switching through an in-plane route because of in-plane FM easy axis. In the R_2 channel, the partial magnetization parallel to the current near H_C would defeat the domain wall scattering and result in valleys in $R_2/R_{\min}$-H.

TABLE I. Integrated area of every Co and Mn 3*d* orbital.

3*d* orbital	*xy*	*xz*	*yz*	x^2–y^2	$3z^2$–r^2
Bulk Co	1.420	1.038	1.369	1.142	1.285
Interfacial Co	1.497	1.350	1.414	1.077	1.412
Bulk Mn	0.876	1.031	1.031	1.045	0.856
Interfacial Mn	0.853	1.022	1.025	1.009	0.888

Such a magnetization switching model explains the MR variation and is also proved by the micromagnetic simulation using 3D object-oriented micromagnetic framework (OOMMF) [18]. According to the resolved AFM structure in XMLD, the interfacial *G*-type AFM structure of the SCO layer is introduced by adding a FM materials layer of $20 \times 80 \times 2\,\text{nm}^3$ on the top of LSMO with a very large perpendicular magnetic anisotropy and magnetic field in the z axis and the magnetization direction of the adjacent cell is opposite. The simulation results of representative areas under different magnetic fields are illustrated in Figs. 7(e) and 7(f) (see full areas in Fig. S7 in [23]). The background color and arrows indicate the magnetization direction: Red background and blue arrow stand for the upward magnetization in the out-of-plane z axis, while the blue background and red arrow denote the downward one. The images in the xy plane view are from LSMO and the top and bottom layers in the xz plane view reflect the magnetization of the SCO and LSMO layers, respectively. When the magnetic field is swept from +5 kOe

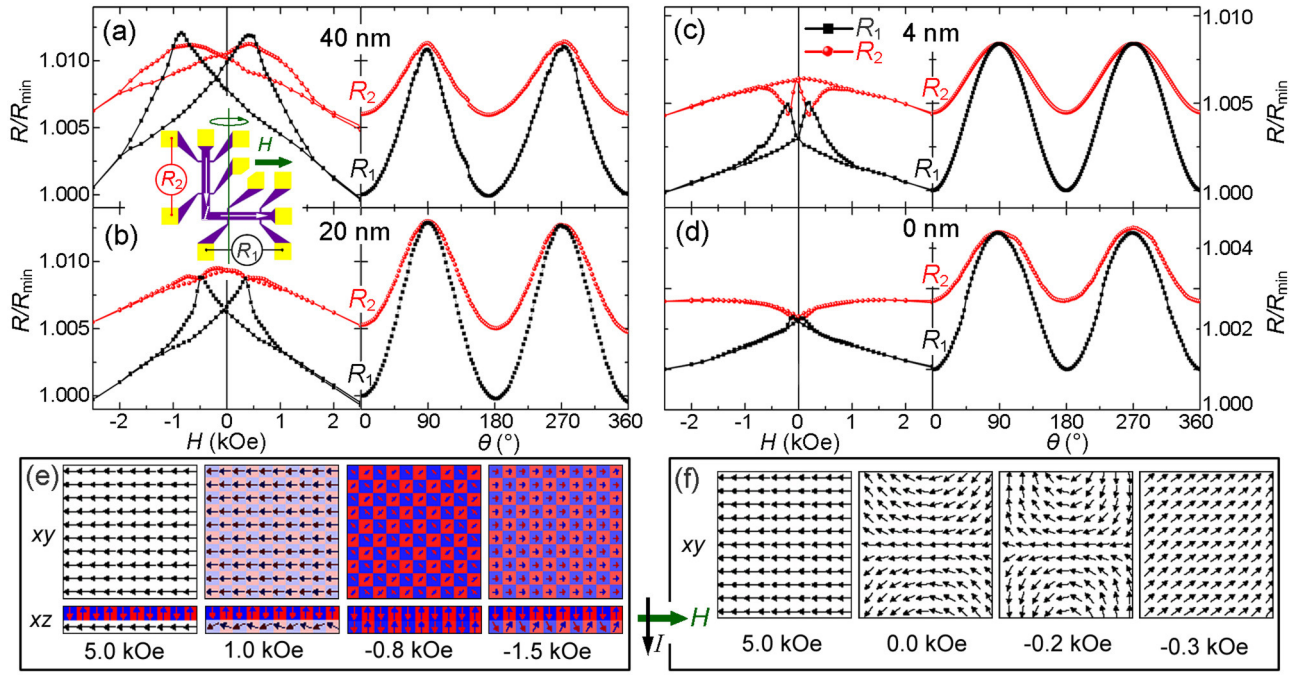

FIG. 7. The R/R_{min}-H (left column) and R/R_{min}-θ (right column) curves for LSMO/SCO orthogonal Hall-bar device [inset of (a)] with different t: (a) 40 nm, (b) 20 nm, (c) 4 nm, and (d) 0 nm. R_1 (black curves) and R_2 (red curves) are the resistances for the channel parallel and perpendicular to the magnetic field. Selected areas of OOMMF simulation for the LSMO layer of (e) LSMO/SCO and (f) single LSMO. The color for the background stands for the magnetization direction along the z axis: White, red, and blue are for the magnetization direction without the z-axis component, in positive and negative z axis, respectively. The top layer of the xz plane view in (e) is taken from SCO. The magnetization of LSMO/SCO switches in an out-of-plane route while that of single LSMO is in an in-plane route under magnetic field.

to –5 kOe along the x axis in SCO/LSMO, the magnetization of LSMO rotates to a perpendicular direction near H_C (darker background color and magnetization perpendicular to the interface) in Fig. 7(e). Different from the out-of-plane magnetization rotation for the SCO/LSMO with the help of perpendicular magnetized SCO, the magnetization of single LSMO is rotated in plane without any pinning effect [Fig. 7(f)]. These simulation results strongly endorse the magnetization switching model of LSMO with (out of plane) and without (in plane) comparatively thick SCO films.

IV. CONCLUSIONS

In summary, the AFM structure with the depth of G-AFM $SrCoO_{2.5}$ is directly illustrated. The AFM structure is demonstrated to be aligned out of plane with a 60° canted angle at the LSMO/SCO interface, then falls to in plane gradually with the distance departing from the interface, and finally returns to the [110] crystal axis in the bulk of the film. The evolution of AFM structure is closely related to the charge transfer from LSMO to SCO and orbital reconstruction from in plane to out of plane. First-principles calculations also reveal the AFM structure evolution manipulated by the electronic reconstruction at the interface in theory. Such an interfacial AFM reconfiguration modulates the magnetization switching process of $La_{2/3}Sr_{1/3}MnO_3$ by reversing the profile of magnetoresistance in turn. Our study not only finds the coupling between charge, orbital, and AFM structure, but also provides a unique approach to controlling the AFM materials.

ACKNOWLEDGMENTS

The authors are grateful to Dr. B. F. Miao and Dr. D. A. Gilbert for fruitful discussions on OOMMF simulation. We acknowledge Beamline BL08U1A in Shanghai Synchrotron Radiation Facility (SSRF) for XAS, XMLD, XLD, and XMCD measurements. This work was supported by the National Natural Science Foundation of China (Grants No. 51322101, No. 51571128, No. 51671110863, and No. 51231004) and Ministry of Science and Technology of the People's Republic of China (Grants No. 2016YFA0203800, No. 2014AA032904, and No. 2014AA032901).

B.C. and F.L. contributed equally to this work.

[1] C. Chappert, A. Fert, and F. N. V. Dau, Nat. Mater. **6**, 813 (2007).

[2] S. S. P. Parkin, C. Kaiser, A. Panchula, P. M. Rice, B. Hughes, M. Samant, and S. H. Yang, Nat. Mater. **3**, 862 (2004).

[3] B. G. Park, J. Wunderlich, X. Martí, V. Holý, Y. Kurosaki, M. Yamada, H. Yamamoto, A. Nishide, J. Hayakawa, H. Takahashi, A. B. Shick, and T. Jungwirth, Nat. Mater. **10**, 347 (2011).

[4] R. O. Cherifi, V. Ivanovskaya, L. C. Phillips, A. Zobelli, I. C. Infante, E. Jacquet, V. Garcia, S. Fusil, P. R. Briddon, N. Guiblin, A. Mougin, A. A. Ünal, F. Kronast, S. Valencia, B. Dkhil, A. Barthélémy, and M. Bibes, Nat. Mater. **13**, 345 (2014).
[5] Y. Y. Wang, X. Zhou, C. Song, Y. N. Yan, S. M. Zhou, G. Y. Wang, C. Chen, F. Zeng, and F. Pan, Adv. Mater. **27**, 3196 (2015).
[6] P. Wadley, B. Howells, J. Zelezn, C. Andrews, V. Hills, R. P. Campion, V. Novak, F. Freimuth, Y. Mokrousov, A. W. Rushforth, K. W. Edmonds, B. L. Gallagher, and T. Jungwirth, Science **351**, 587 (2016).
[7] H. Y. Hwang, Y. Iwasa, M. Kawasaki, B. Keimer, N. Nagaosa, and Y. Tokura, Nat. Mater. **11**, 103 (2012).
[8] A. Tebano, C. Aruta, S. Sanna, P. G. Medaglia, G. Balestrino, A. A. Sidorenko, R. De Renzi, G. Ghiringhelli, L. Braicovich, V. Bisogni, and N. B. Brookes, Phys. Rev. Lett. **100**, 137401 (2008).
[9] J. Garcia-Barriocanal, J. C. Cezar, F.Y. Bruno, P. Thakur, N. B. Brookes, C. Utfeld, A. Rivera-Calzada, S. R. Giblin, J. W. Taylor, J. A. Duffy, S. B. Dugdale, T. Nakamura, K. Kodama, C. Leon, S. Okamoto, and J. Santamaria, Nat. Commun. **1**, 82 (2010).
[10] C. He, A. J. Grutter, M. Gu, N. D. Browning, Y. Takamura, B. J. Kirby, J. A. Borchers, J. W. Kim, M. R. Fitzsimmons, X. Zhai, V. V. Mehta, F. J. Wong, and Y. Suzuki, Phys. Rev. Lett. **109**, 197202 (2012).
[11] S. M. Wu, S. A. Cybart, P. Yu, M. D. Rossell, J. X. Zhang, R. Ramesh, and R. C. Dynes, Nat. Mater. **9**, 756 (2010).
[12] B. Cui, C. Song, G. A. Gehring, F. Li, G. Y. Wang, C. Chen, J. J. Peng, H. J. Mao, F. Zeng, and F. Pan, Adv. Funct. Mater. **25**, 864 (2015).
[13] P. Yu, J.-S. Lee, S. Okamoto, M. D. Rossell, M. Huijben, C.-H. Yang, Q. He, J. X. Zhang, S. Y. Yang, M. J. Lee, Q. M. Ramasse, R. Erni, Y.-H. Chu, D. A. Arena, C.-C. Kao, L. W. Martin, and R. Ramesh, Phys. Rev. Lett. **105**, 027201 (2010).
[14] C. Becher, L. Maurel, U. Aschauer, M. Lilienblum, C. Magén, D. Meier, E. Langenberg, M. Trassin, J. Blasco, I. P. Krug, P. A. Algarabel, N. A. Spaldin, J. A. Pardo, and M. Fiebig, Nat. Nanotechnol. **10**, 661 (2015).
[15] S. J. Callori, S. Hu, J. Bertinshaw, Z. J. Yue, S. Danilkin, X. L. Wang, V. Nagarajan, F. Klose, J. Seidel, and C. Ulrich, Phys. Rev. B **91**, 140405(R) (2015).
[16] A. Muñoz, C. de la Calle, J. A. Alonso, P. M. Botta, V. Pardo, D. Baldomir, and J. Rivas, Phys. Rev. B **78**, 054404 (2008).
[17] F. Li, C. Song, Y. Y. Wang, B. Cui, H. J. Mao, J. J. Peng, S. N. Li, and F. Pan, Phys. Rev. B **93**, 024406 (2016).
[18] S. R. Bakaul, W. Hu, T. Wu, and T. Kimura, Phys. Rev. B **86**, 184404 (2012).
[19] Y. Takamura, E. Folven, J. B. R. Shu, K. R. Lukes, B. Li, A. Scholl, A. T. Young, S. T. Retterer, T. Tybell, and J. K. Grepstad, Phys. Rev. Lett. **111**, 107201 (2013).
[20] M. Ali, C. H. Marrows, and B. J. Hickey, Phys. Rev. B **67**, 172405 (2003).
[21] E. Arenholz, G. van der Laan, R. V. Chopdekar, and Y. Suzuki, Phys. Rev. B **74**, 094407 (2006).
[22] S. Czekaj, F. Nolting, L. J. Heyderman, P. R. Willmott, and G. van der Laan, Phys. Rev. B **73**, 020401(R) (2006).
[23] See Supplemental Material at http://link.aps.org/supplemental/10.1103/PhysRevB.94.134403 for the details of SCO electronic structure, XMLD, XMCD, first-principles calculations, and OOMMF simulation.
[24] S. Dong, K. Yamauchi, S. Yunoki, R. Yu, S. H. Liang, A. Moreo, J.-M. Liu, S. Picozzi, and E. Dagotto, Phys. Rev. Lett. **103**, 127201 (2009).
[25] F. Li, C. Song, Y. Y. Wang, B. Cui, H. J. Mao, J. J. Peng, S. N. Li, G. Y. Wang, and F. Pan, Sci. Rep. **5**, 16187 (2015).
[26] H. Jeen, W. S. Choi, M. D. Biegalski, C. M. Folkman, I. C. Tung, D. D. Fong, J. W. Freeland, D. W. Shin, H. Ohta, M. F. Chisholm, and H. N. Lee, Nat. Mater. **12**, 1057 (2013).
[27] B. Cui, C. Song, H. J. Mao, H. Q. Wu, F. Li, J. J. Peng, G. Y. Wang, F. Zeng, and F. Pan, Adv. Mater. **27**, 6651 (2015).
[28] S. X. Wu, X. Luo, S. Turner, H. Y. Peng, W. N. Lin, J. F. Ding, A. David, B. Wang, G. Van Tendeloo, J. L. Wang, and T. Wu, Phys. Rev. X **3**, 041027 (2013).
[29] B.-Y. Wang, J.-Y. Hong, K.-H. O. Yang, Y.-L. Chan, D.-H. Wei, H.-J. Lin, and M.-T. Lin, Phys. Rev. Lett. **110**, 117203 (2013).
[30] G. J. Snyder, M. R. Beasley, T. H. Geballe, R. Hiskes, and S. DiCarolis, Appl. Phys. Lett. **69**, 4254 (1996).
[31] B. Cui, C. Song, Y. Sun, Y. Y. Wang, Y. L. Zhao, F. Li, G. Y. Wang, F. Zeng, and F. Pan, Appl. Phys. Lett. **105**, 152402 (2014).
[32] Q. Li, H. S. Wang, Y. F. Hu, and E. Wertz, J. Appl. Phys. **87**, 5573 (2000).
[33] R. W. Li, H. B. Wang, X. W. Wang, X. Z. Yu, Y. Matsui, Z. H. Cheng, B. G. Shen, E. W. Plummer, and J. D. Zhang, Proc. Natl. Acad. Sci. U. S. A. **106**, 14224 (2009).